Crystal Structure of Feline Infectious Peritonitis Virus Main Protease in Complex with Synergetic Dual Inhibitors

Fenghua Wang,[a] Cheng Chen,[a,b] Xuemeng Liu,[c] Kailin Yang,[d] Xiaoling Xu,[c] Haitao Yang[a,b]

School of Life Sciences, Tianjin University, Tianjin, People's Republic of China[a]; Tianjin International Joint Academy of Biotechnology and Medicine, Tianjin, People's Republic of China[b]; Institute of Ageing Research, School of Medicine, Hangzhou Normal University, Hangzhou, China[c]; Cleveland Clinic Lerner College of Medicine of Case Western Reserve University, Cleveland, Ohio, USA[d]

ABSTRACT

Coronaviruses (CoVs) can cause highly prevalent diseases in humans and animals. Feline infectious peritonitis virus (FIPV) belongs to the genus *Alphacoronavirus*, resulting in a lethal systemic granulomatous disease called feline infectious peritonitis (FIP), which is one of the most important fatal infectious diseases of cats worldwide. No specific vaccines or drugs have been approved to treat FIP. CoV main proteases (M^{pro}s) play a pivotal role in viral transcription and replication, making them an ideal target for drug development. Here, we report the crystal structure of FIPV M^{pro} in complex with dual inhibitors, a zinc ion and a Michael acceptor. The complex structure elaborates a unique mechanism of two distinct inhibitors synergizing to inactivate the protease, providing a structural basis to design novel antivirals and suggesting the potential to take advantage of zinc as an adjunct therapy against CoV-associated diseases.

IMPORTANCE

Coronaviruses (CoVs) have the largest genome size among all RNA viruses. CoV infection causes various diseases in humans and animals, including severe acute respiratory syndrome (SARS) and Middle East respiratory syndrome (MERS). No approved specific drugs or vaccinations are available to treat their infections. Here, we report a novel dual inhibition mechanism targeting CoV main protease (M^{pro}) from feline infectious peritonitis virus (FIPV), which leads to lethal systemic granulomatous disease in cats. M^{pro}, conserved across all CoV genomes, is essential for viral replication and transcription. We demonstrated that zinc ion and a Michael acceptor-based peptidomimetic inhibitor synergistically inactivate FIPV M^{pro}. We also solved the structure of FIPV M^{pro} complexed with two inhibitors, delineating the structural view of a dual inhibition mechanism. Our study provides new insight into the pharmaceutical strategy against CoV M^{pro} through using zinc as an adjuvant therapy to enhance the efficacy of an irreversible peptidomimetic inhibitor.

Coronaviruses (CoVs) infect humans and animals, causing various highly prevalent and severe diseases, such as severe acute respiratory syndrome (SARS) and Middle East respiratory syndrome (MERS) (1, 2). Feline infectious peritonitis virus (FIPV) belongs to the genus *Alphacoronavirus* in the subfamily *Coronavirinae*. It is a highly virulent mutant of the feline enteric coronavirus (FECV), which is closely related to transmissible gastroenteritis coronavirus (TGEV) of pigs and canine coronavirus (CCV) (3). In contrast with FECV, which causes asymptomatic or mild infection in cats and other felines, FIPV is an etiologic agent resulting in a lethal systemic granulomatous disease called feline infectious peritonitis (FIP), one of the most important fatal infectious diseases of cats worldwide (4). There are no effective drugs specific for FIP. The development of vaccines toward FIPV has also failed due to the antibody-dependent enhancement, where infection of the monocyte/macrophage lineage by FIPV is enhanced in the presence of antibodies (5). Thus, discovery of effective antivirals against FIPV is desired for the treatment of FIP.

Similar to other alphacoronaviruses, FIPV contains a single positive-stranded RNA genome that is composed of two overlapping open reading frames (ORFs), ORF1a and ORF1b at the 5' end, encoding two large polyproteins, pp1a and pp1ab (6). These two polyproteins are subsequently cleaved into 16 nonstructural proteins (nsp1 to nsp16), which assemble into a membrane-anchored replication machinery for transcription/replication. Cleavage is regulated by two proteases: the main protease (M^{pro},

also called nsp5 or 3C-like protease), and the papain-like protease (PL^{pro}). PL^{pro} processes the N-terminal end of pp1a/pp1ab into nsp1, nsp2, and nsp3, while M^{pro} cleaves the polyproteins at 11 sites to release nsp4 to nsp16 (6). The essential roles M^{pro} plays in the viral life cycle and the lack of a cellular homologue in the human genome make it an attractive target for drug design.

To date, several crystal structures of CoV M^{pro} and the complex of M^{pro}-inhibitor have been determined (7–16). However, the 3-dimensional structure of FIPV M^{pro} is still unavailable, deterring rational drug design against FIP. Although extensive mutagenesis studies have been carried out to probe the hydrolysis mechanism of FIPV M^{pro} (17), a *bona fide* structural model is needed to interpret the enzymatic data. Here, we report the crystal structure of FIPV M^{pro} in complex with synergetic dual inhibitors,

a Michael acceptor inhibitor (an α,β-unsaturated ester) named N3 and a metal ion, Zn^{2+}. The complex structure provides structural fundamentals for designing novel antiviral strategies against FIP and other CoV-relevant diseases.

MATERIALS AND METHODS

Protein expression, purification, and crystallization. The expression and purification of FIPV main protease have been described previously (18). Briefly, the coding sequence for FIPV M^{pro} was cloned into the vector pGEX-6P-1 and transformed into *Escherichia coli* strain BL21(DE3) for protein expression. Cultures were grown in LB medium at 310 K and then induced by 0.5 mM isopropyl-β-D-thiogalactopyranoside at 289 K. The glutathione S-transferase (GST) fusion protein, GST-FIPV M^{pro}, was purified by GST-glutathione affinity chromatography and cleaved with rhinovirus 3C protease. M^{pro} was further purified by using anion exchange chromatography and size exclusion chromatography. The inhibitor N3 was added to the purified protein with a molar ratio of 3:1 to 5:1. Crystallization trials were set up in 16-well crystallization plates at 291 K using the hanging-drop vapor diffusion method. The optimized conditions for crystal growth consisted of 0.2 M zinc acetate dihydrate, 0.1 M sodium cacodylate trihydrate, pH 6.5, 14% (wt/vol) polyethylene glycol 8000.

Crystal data collection, structure determination, and refinement. Crystals were cryoprotected with 20% glycerol added to the reservoir solution and flash-frozen with liquid nitrogen. A 2.8-Å resolution data set was collected at 100 K using an ADSC Q315r detector on beamline BL17U of the Shanghai Synchrotron Radiation Facility (SSRF) with a wavelength of 0.97923 Å. The crystal belongs to space group *I*422, with unit cell dimensions *a* = *b* = 112.3 Å, *c* = 102.1 Å. The diffraction data were processed, integrated, and scaled with HKL2000 (19). The structure of M^{pro} was solved by molecular replacement using the structure of TGEV M^{pro} (PDB code 2AMP) as a search model through the PHASER (20) program from the CCP4 package (21). Iterative model building and refinement were performed using PHENIX (22) to obtain the final model, with R_{work} of 21.2% and R_{free} of 24.3% at 2.8-Å resolution.

Enzyme activity and inhibition assays. The activity of M^{pro} and inhibition of N3 were measured by continuous kinetic assays, using the fluorogenic substrate MCA-AVLQSGFR-Lys(Dnp)-Lys-NH2 (>95% purity) (GL Biochem Shanghai Ltd., Shanghai, China), which was from the N-terminal autocleavage site of SARS-CoV M^{pro}, as previously reported (23).

The kinetic parameters for Zn^{2+} inhibition were evaluated using equation 1 (24), where K_i is the dissociation constant for the FIPV M^{pro} complexed with Zn^{2+} and factor α reflects the effect of the inhibitor on the affinity of the enzyme for its substrate, v is initial velocity, [S] is substrate concentration, and [I] is concentrations of an inhibitor:

$$v = \frac{V_{max}[S]}{[S]\left(1 + \frac{[I]}{\alpha K_i}\right) + K_m\left(1 + \frac{[I]}{K_i}\right)} \quad (1)$$

The values of V_{max} and K_m at different Zn^{2+} concentrations were the apparent V_{max} and K_m, hereinafter denoted V_{max}^{app} and K_m^{app}, respectively. According to equation 1, V_{max}^{app} and K_m^{app} can be calculated by equation 2:

$$V_{max}^{app} = \frac{V_{max}}{1 + \frac{[I]}{\alpha K_i}}, \quad K_m^{app} = \frac{K_m\left(1 + \frac{[I]}{K_i}\right)}{1 + \frac{[I]}{\alpha K_i}} \quad (2)$$

The kinetic parameters of V_{max}^{app} and K_m^{app} were determined by adding 1 μM FIPV M^{pro} to 40 μM substrate containing various concentrations of zinc ion (0 to 4 μM) (24). The value of αK_i was then calculated from plots of $1/V_{max}^{app}$ versus [I]. Similarly, the value of K_i was calculated from plots of K_m^{app}/V_{max}^{app} versus [I].

Protein structure accession number. The atomic coordinates and structure factors of the FIPV M^{pro}-Zn^{2+}-N3 complex have been deposited in the Protein Data Bank with the accession code 5EU8.
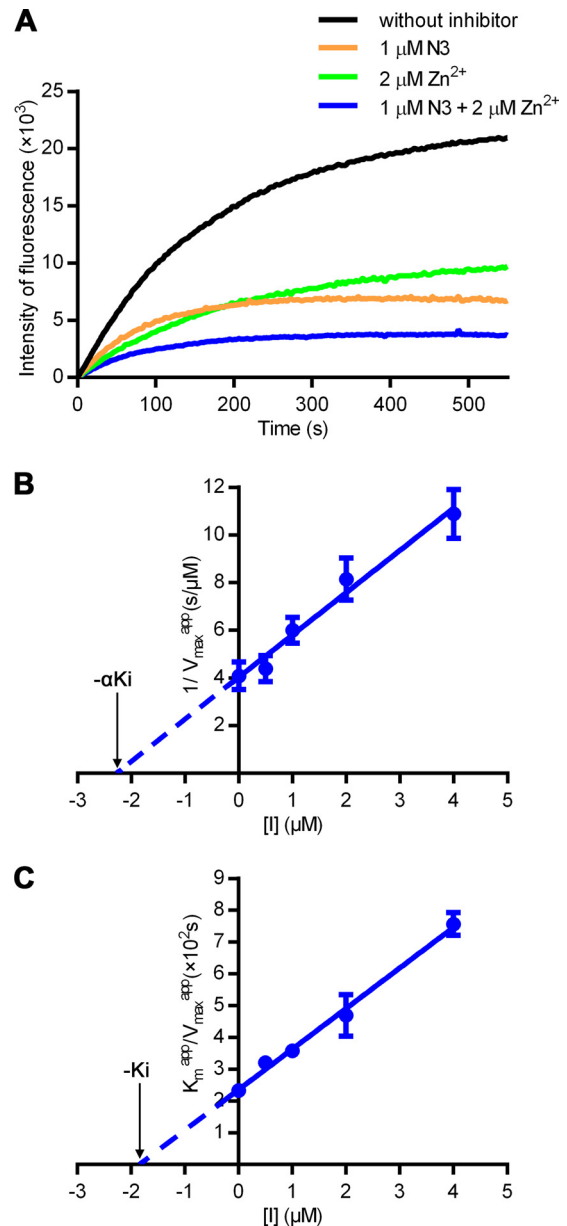
FIG 1 Synergetic inhibition of FIPV M^{pro} by Zn^{2+} and N3. (A) Inhibition of FIPV M^{pro} by different compounds. Fluorescence curve of FIPV M^{pro} free of inhibitors (black) or with 1 μM N3 (orange), 2 μM Zn^{2+} (green), or the dual inhibitors (blue), respectively. The fluorescence intensity is plotted against time to represent enzyme activity. (B and C) Secondary plots to determine the kinetic constants (αK_i and K_i) of Zn^{2+} as a noncompetitive inhibitor. The values of αK_i (B) and K_i (C) are calculated from the x intercept.

RESULTS

Discovery of synergetic inhibition of FIPV M^{pro} by Zn^{2+} and N3. The structure of FIPV M^{pro} has long been awaited for structure-based rational drug design against FIP. In contrast, the crystal structure of TGEV M^{pro}, which shows 93% sequence identity to FIPV M^{pro}, was solved more than a decade ago. We have screened thousands of crystallization conditions for FIPV M^{pro} but failed to obtain crystals, implying that the intrinsic flexibility of FIPV M^{pro} may prevent crystal formation. Previously, we have designed an α,β-unsaturated ester named N3, which is a mechanism-based
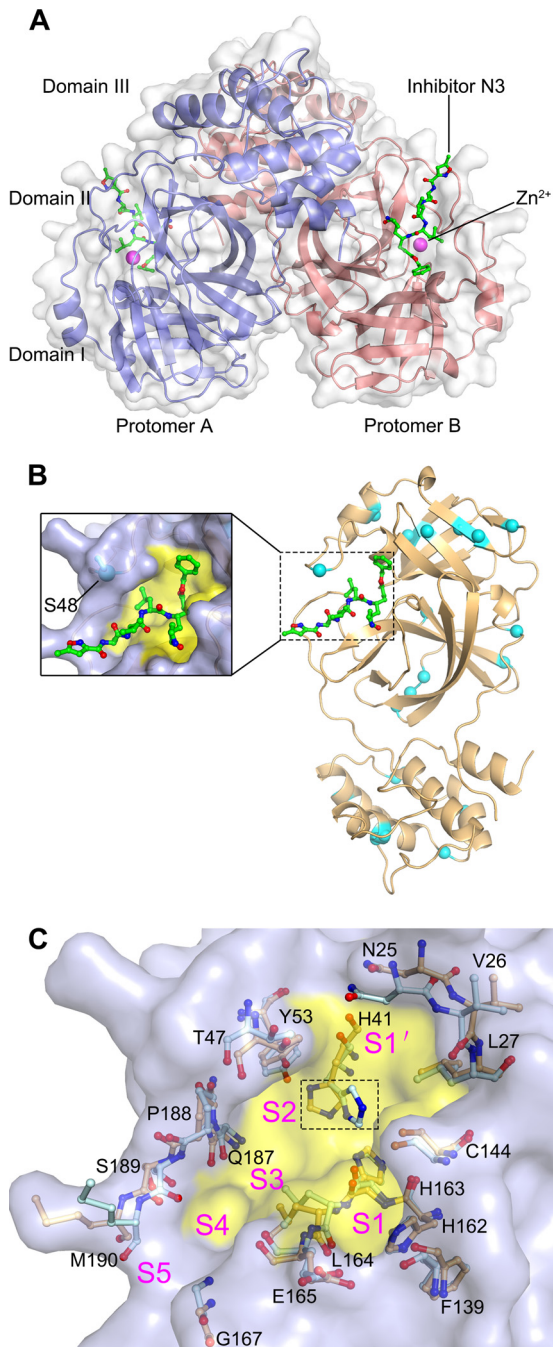
FIG 2 The structure of FIPV M^pro. (A) Overall structure of the FIPV M^pro-Zn^{2+}-N3 complex in surface representation. The two protomers are colored slate and deep salmon, inhibitor N3 is shown as green sticks, and Zn^{2+} is shown as a magenta sphere. (B) Distribution of the nonconserved residues between FIPV and TGEV M^pros. The structure of FIPV M^pro is shown in cartoon representation (light orange). The nonconserved residues between FIPV M^pro and TGEV M^pro are shown as cyan spheres. The N3 molecule is shown as green sticks, and the substrate-binding pocket is colored in yellow. A zoomed view of the substrate-binding pocket is shown to the left. (C) Superimposition of the substrate-binding pocket of FIPV M^pro-Zn^{2+}-N3 (light orange) with that of TGEV M^pro (pale cyan). The substrate-binding pocket of the FIPV M^pro complex is colored in yellow. The S1, S2, S4, S5, and S′ subsites are labeled. The key amino acids constituting the substrate-binding pockets of FIPV M^pro and TGEV M^pro are shown as sticks. The His41 residues specifically are marked by the dashed rectangular box.

irreversible inhibitor, to inhibit multiple CoV M^pros. It could potently inhibit FIPV M^pro with a high inactivation rate ($k_{obs}/[I] = 47{,}000$ M$^{-1} \cdot$ s^{-1}; k_{obs} is the observed first-order inhibition rate constant determined experimentally) (23). Thus, we prepared CoV M^pro complexed with N3 in order to stabilize FIPV M^pro for crystallization. Surprisingly, the complex crystals only grew with the presence of zinc acetate in the reservoir solution, suggesting that zinc ion might act as a cofactor/inhibitor for FIPV M^pro. To investigate the potential effect of zinc ion on the protease, a fluorescence-labeled substrate, MCA-AVLQ ↓ SGFR-Lys(Dnp)-Lys-NH2, was synthesized to determine the kinetic parameters (23). Enzymatic inhibition assays showed that Zn^{2+} could inactivate FIPV M^pro independent of N3 in the low micromolar range (Fig. 1A). Strikingly, the fluorescence curves decreased dramatically in the presence of both Zn^{2+} and N3 compared with the curves in the presence of each alone, suggesting that these two inhibitors could synergistically disable FIPV M^pro, possibly by targeting different binding sites. We then determined the kinetic parameters of Zn^{2+} for inhibiting FIPV M^pro ($\alpha K_i = 2.28$ μM and $K_i = 1.84$ μM), which indicated that Zn^{2+} acts as a noncompetitive reversible inhibitor (Fig. 1B and C).

Overall structure of FIPV M^pro in complex with N3 and Zn^{2+}. In order to investigate the mechanism of how Zn^{2+} and N3 synergistically inhibit FIPV M^pro, we sought to determine the ternary structure of the M^pro-Zn^{2+}-N3 complex. The complex structure was solved by molecular replacement, and the final model is refined to an R_{work}/R_{free} ratio of 21.2%/24.3% at 2.8-Å resolution. The final model contains the full-length FIPV M^pro amino acid sequence (Ser1 to Val299), inhibitor N3, and a zinc ion (Fig. 2A and Table 1). Only one FIPV M^pro molecule can be found in the asymmetric unit. Two symmetric FIPV M^pro molecules associate into a homodimer through domain III and its N terminus (Fig. 2A).

TABLE 1 Refinement statistics[a]

Statistics	Value for the FIPV M^pro-N3-Zn^{2+} complex
Resolution range (Å)	50.0–2.45
No. of reflections	12,061
R_{work} (%)	21.2
R_{free} (%)[b]	24.3
No. of atoms	
Protein	2,301
Water	110
Ligands	54
B factors	
Protein	54.4
Water	48.8
Ligands	64.3
RMS deviations	
Bond length (Å)	0.012
Bond angle (°)	1.23
Ramachandran plot	
Favored regions (%)	97.0
Allowed regions (%)	3.0
Outliers (%)	0.0

[a] Refinement statistics were calculated with the table one utility of PHENIX.
[b] R_{free} was calculated with 5% of the reflection data.
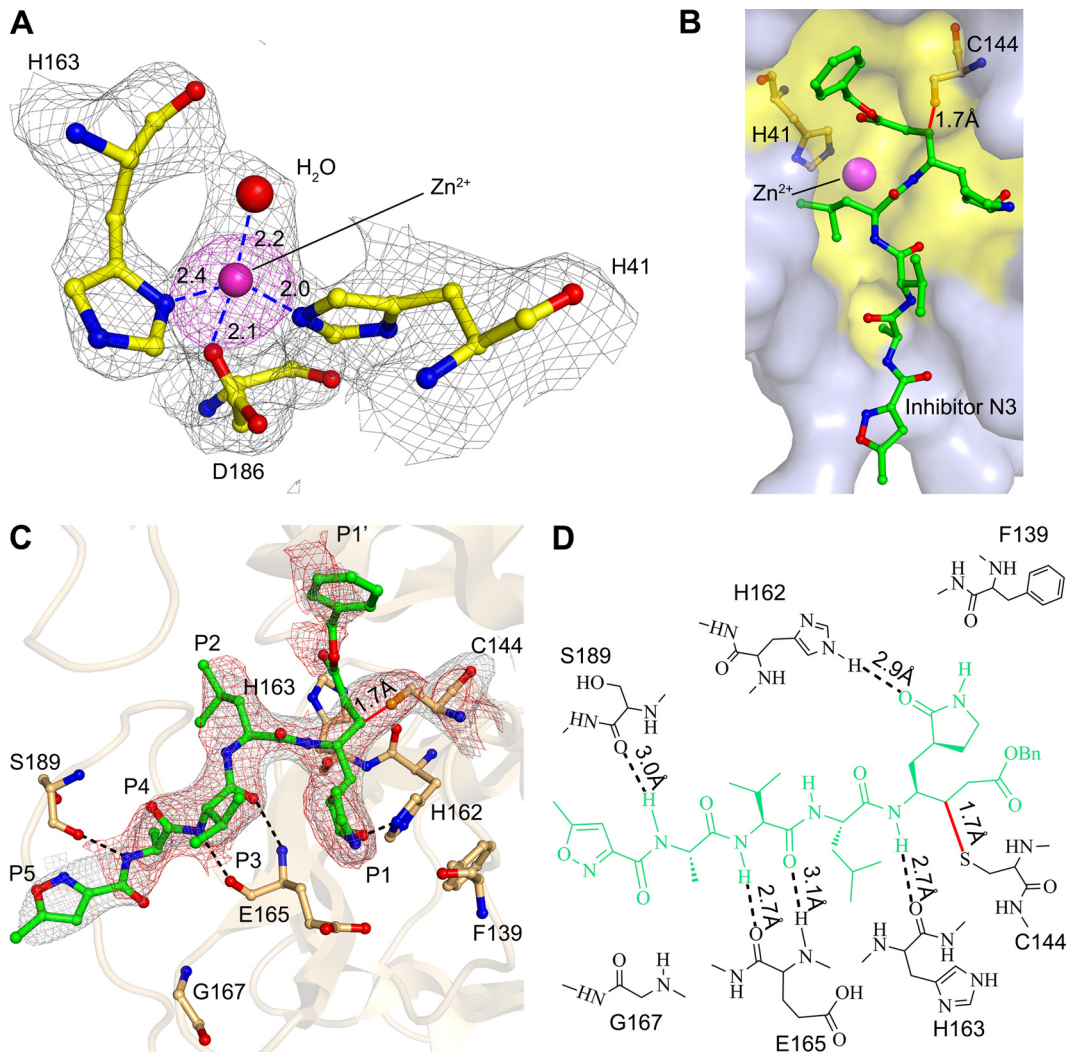
FIG 3 Interactions between N3, Zn^{2+}, and FIPV M^{pro}. (A) Coordination of the Zn^{2+} to the active center of FIPV M^{pro}. A simulated annealing mFo-DFc omit map for unbiased electron density shows the residues and Zn^{2+} in gray at 1 σ, and an anomalous difference Fourier map shows Zn^{2+} in magenta at 3 σ. The hydrogen bonds are displayed as dashed lines, and the distances are labeled in Å. (B) Surface representation of N3 and Zn^{2+} bound to the active site of FIPV M^{pro}. N3 is shown as sticks (green), and the substrate-binding pocket is colored in yellow. The catalytic dyad His41 and Cys144 are shown as light-orange sticks. (C) Interactions between the inhibitor N3 and FIPV M^{pro}. N3 and the key residues are shown as sticks. A sigma-sA-weighted 2mFo-DFc electron density map shows N3 in gray at 1 σ, and a simulated annealing 2mFo-DFc omit map shows N3 in red at 1 σ, respectively. The hydrogen bonds are shown by dashed lines, and the covalent bond by a solid line. The P1, P2, P4, P5, and P1′ sites are labeled. (D) Detailed view of the interactions between the inhibitor N3 and FIPV M^{pro}. The N3 inhibitor is shown in green. Hydrogen bonds are shown by dashed lines, and the covalent bond is a red solid line.

Reminiscent of other solved M^{pro} structures, each monomer contains three domains: domains I and II are mainly composed of antiparallel β-barrels and domain III is formed by five α-helices. The inhibitor N3 lies in the substrate-binding pocket located between domains I and II. Zn^{2+} could be found adjacent to N3 (Fig. 2A).

FIPV M^{pro} and TGEV M^{pro} have an identical substrate-binding pocket. Compared with FIPV, TGEV is a swine CoV that causes transmissible gastroenteritis in pigs. Although the hosts and pathogenesis of the two viruses are distinct from each other, they both belong to genus *Alphacoronavirus*, based on their genomic sequence identity. Specifically, sequence alignment shows that only 7% (21 of 302) of the residues are not conserved between the TGEV and FIPV M^{pro}s. Although the nonconserved residues are distributed throughout the whole structure (Fig. 2B),

the residues involved in substrate binding are identical between the two proteases (Fig. 2C). This implies that the overall substrate-binding pockets of FIPV and TGEV M^{pro}s remain intact during evolution and that these two proteases have the same substrate preference. This interesting finding suggests that a drug targeting the active site of either of the two viral proteases should be as effective for the other.

Interaction between Zn^{2+} and FIPV M^{pro}. The zinc ion has been identified in the active site of FIPV M^{pro}, which is coordinated by Nδ1 of His163, Nε2 of His41, Oδ1 of Asp186, and a water molecule (Fig. 3A). As the residues involved in substrate binding are identical between FIPV and TGEV M^{pro}s, the apo form of TGEV M^{pro} (10) was overlaid with that of FIPV to address the conformational changes imposed by Zn^{2+} binding (Fig. 2C). Superimposition of the FIPV M^{pro} complex and apo-TGEV M^{pro} has
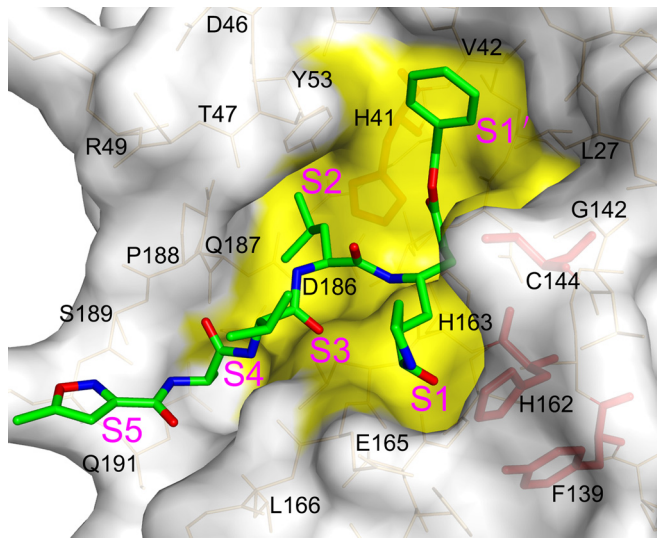
FIG 4 Structural insight into the mutagenesis analysis of the FIPV M^pro active center. Surface representation of FIPV M^pro complexed with inhibitor N3. The substrate-binding pocket is colored in yellow. The N3 molecule is shown as green sticks. Residues His41, Cys144, Tyr160, and His162 are shown as red sticks.

shown that although the root mean square deviation (RMSD) for the whole Cα atoms is 0.74 Å, the configuration of the key residues constituting the substrate-binding pockets of FIPV M^pro and TGEV M^pro is still well matched, except for His41 (Fig. 2C). It shows that upon Zn^{2+} binding, Nε2 of His41 shifted ~4 Å away from the active site and then participated in coordinating the metal ion. His41 and Cys144 are the catalytic dyad for CoV M^pro's. Nε2 of His41 is responsible for accepting the proton from the thiol group of Cys144 and then initiating a nucleophilic attack on the peptide bond. Due to the interaction with Zn^{2+}, the distance between Nε2 of His41 and the thiol group of Cys144 increased from 4 Å in apo M^pro to ~8 Å in the M^pro-Zn^{2+} complex, preventing efficient transfer of the proton from Cys144 to the imidazole ring of His41 (Fig. 2C and 3B). In addition, we noticed that the relocation of His41 made sufficient room for accommodating the bulky benzyl group of N3 (Fig. 3B).

Interaction between FIPV M^pro and N3. The inhibitor N3 is located at the cleft between domains I and II of FIPV M^pro, with a buried surface area of 679 Å² (~70% of its total surface area). The Sγ atom of Cys144 is covalently bound to Cβ of the vinyl group of N3 by a 1.7-Å C-S bond due to a nucleophilic reaction (Fig. 3C and D). The inhibitor is stabilized by a hydrogen bond network through interacting with the imidazole ring of His162, main chain of His163, amide group of Glu165, and carbonyl oxygen of Ser189 (Fig. 3C and D). In detail, the lactam at the P1 site of N3 favorably inserts into the S1 pocket, consisting of side chains of residues Phe139, His162, His163, Glu165, and His171 (Fig. 4). The side chain of Leu at the P2 site stretches into the hydrophobic S2 pocket formed by His41, Thr47, Tyr53, Asp186, Gln187, and Pro188 (Fig. 4). In contrast, the P3 site of N3 faces the solvent. The P4 and P5 sites of N3 are surrounded by two loops: loop 1 (residues 188 to 191) and loop 2 (residues 165 to 167). In addition, the benzyl ester at the P1′ site of N3 makes an extensive contact with residues constituting the hydrophobic S1′ pocket, including Asn25, Val26, Leu27, His41, Val42, and Thr47 (Fig. 4).

Structural insight into the mutagenesis analysis of FIPV M^pro's active center. Both the catalytic mechanism and substrate-binding pocket of FIPV M^pro have been thoroughly studied by site-directed mutagenesis prior to its crystal structural analysis. A couple of critical residues were found to be indispensable for its proteolytic activity (Table 2) (17), and yet, a *bona fide* model of FIPV M^pro is needed to analyze the accumulated enzymatic data.

It is not surprising that mutants H41Y (with an H-to-Y mutation at position 41), H41R, and C144A completely lost their activity, given the essential role of His41 and Cys144 in proteolytic function. In the crystal structure, His41 and Cys144 form a catalytic dyad, of which His41 acts as a base and proton acceptor, whereas Cys144 initiates a nucleophilic attack on the peptide bond. C144S was found to be inactive, demonstrating that appropriate nucleophilicity is important to promote a nucleophilic attack for this cysteine protease. No obvious activity could be detected for H162A and H162L. This is because His162 is a critical component for the substrate-binding pocket, particularly the S1 subsite (Fig. 4). Nε2 of H162 was seen to form a hydrogen bond with the lactam oxygen of N3, suggesting its important role in substrate recognition. Y160A and Y160T mutants are almost inactive. This can be explained by the fact that even though Tyr160 is not directly involved in substrate binding, the hydroxyl oxygen of its side chain interacts with Nδ1 of His162 through a 3.0-Å hydrogen bond, helping to maintain an appropriate conformation of the substrate-binding pocket.

DISCUSSION

FIP is one of the most frequently fatal infectious diseases of cats. Unfortunately, the development of effective vaccines against the pathogen FIPV has failed due to antibody-dependent enhancement (5). M^pro of CoV has been commonly accepted as an ideal drug target, but the development of inhibitors against FIPV M^pro has progressed slowly in the past due to the lack of *bona fide* structural models. In this study, we were able to determine its crystal structure only in the presence of a zinc ion and a Michael acceptor inhibitor, implying that these two factors function to circumvent the intrinsic flexibility of the protease that prevents crystal packing.

The Michael acceptor N3 binds to FIPV M^pro in a canonical mode, as in other M^pro structures. N3 is known to inactivate FIPV M^pro efficiently and to possess potent antiviral activity in cell-based assays (17), but the molecular mechanism has not been fully

TABLE 2 Mutagenesis analysis of the FIPV M^pro active center

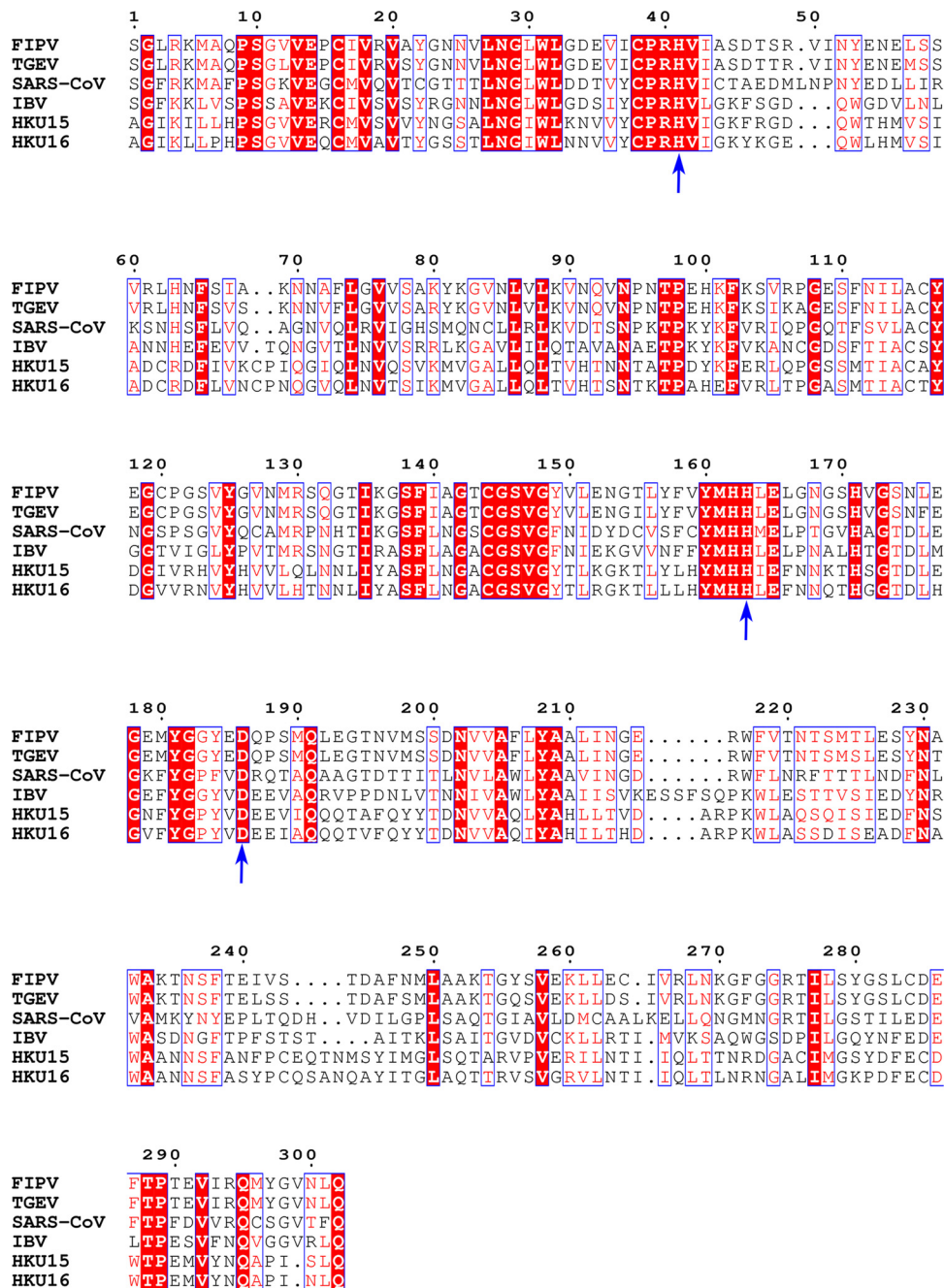| Structure-activity relationship	Mutation	Activity (%)
Nucleophile	C144A	<1
	C144S	<1
Proton acceptor	H41Y	<1
	H41R	<1
Constituting the substrate-binding pocket	H162A	<1
	H162L	<1
Stabilizing the substrate-binding pocket	Y160G	4
	Y160F	3
	Y160A	1
	Y160T	<1

[a] Data are from reference 17.

FIG 5 Sequence alignment of the M^{pro}s from different CoVs. FIPV (GenBank accession no. AY994055) and TGEV (GenBank accession no. FJ755618) are from *Alphacoronavirus*, SARS-CoV (GenBank accession no. NC_004718) from *Betacoronavirus*, infectious bronchitis virus (IBV) (GenBank accession no. AY641576) from *Gammacoronavirus*, and porcine coronavirus HKU15 (GenBank accession no. KM012168) and white-eye coronavirus HKU16 (GenBank accession no. NC_016991) from *Deltacoronavirus*. The conserved residues that participate in coordinating the Zn^{2+} are labeled by arrows. Sequence alignment was performed with ClustalW and drawn using ESPript3. White letters with red backgrounds show identical residues, and red letters with white backgrounds show conservative variation. Blue arrows indicate residues involved in coordinating Zn^{2+} in FIPV M^{pro} and are well-conserved in M^{pro} sequences from multiple species.

elucidated. The structural information provided here will contribute to the development of more efficacious antivirals against FIPV, as well as TGEV, since these two M^{pro}s share identical residues in the substrate-binding pocket.

To our surprise, a Zn^{2+} ion has also been identified in the ternary structure of the M^{pro}-Zn^{2+}-N3 complex. As the second most abundant physiological transition metal ion in the human body (25), Zn^{2+} could play totally contrary roles in affecting the enzymatic activity of proteases. On one hand, for example, the metzincin superfamily is a group of proteases that are distinguished by a highly conserved motif containing three histidines to bind Zn^{2+} at the catalytic site for the enzyme activity (26). On the other hand, Zn^{2+} has also been reported to inhibit serine/cysteine proteases (27), which could be seen in our case as well.

In our structure, Zn^{2+} and the inhibitor N3 demonstrated a unique mode of independent but synergetic inhibition, distinct from the Zn^{2+}-dependent inhibition of trypsin by bis(5-amidino-2-benzimidazolyl)methane (BABIM), in which a Zn^{2+} ion (a very weak inhibitor) bridges BABIM (also a very weak inhibitor) and the active site of trypsin to impose potent inhibition (27). The Zn^{2+} ion itself plays triple roles here: (i) it blocks efficient transfer of the proton from the catalytic residue for nucleophilic attack; (ii) it prevents the protonation of the catalytic residue that is supposed to accept the proton; and (iii) it induces rearrangement of the substrate-binding pocket to better accommodate the functional group of another inhibitor. Additionally, His163, His41, and Asp186, which participate in coordinating the Zn^{2+} in FIPV M^{pro}, are well conserved in multiple species of M^{pro}s (Fig. 5), suggesting that Zn^{2+} can broadly inhibit CoV M^{pro}s. This is consistent with a previous report that Zn^{2+} could inhibit SARS-CoV M^{pro} (12).

As an abundant physiological transition metal ion in the human body, the plasma concentration of zinc ranges from 10 to 20 μM (25). Because most of the zinc is protein bound, the concentration of unbound or free ion is only 0.5 to 1 μM, which is actually low. However, the plasma concentration of zinc is not static and can change under certain conditions. In the milieu of activation, the free zinc concentrations can reach 7 to 10 μM (25, 28). This suggests that it could be plausible to consider the therapeutic value of zinc. In fact, zinc has been used to treat the common cold since 1984, but the effect of this treatment has been controversial for a long time (29, 30). Most recent and systematic trials have shown that the intake of zinc was indeed associated with a significant reduction in the duration of days of cold symptoms (31, 32). The rationale for zinc treatment of the common cold can possibly be attributed to its antagonistic effect on the rhinovirus 3C protease, an essential enzyme for rhinovirus replication (33). Although rhinovirus is the significant contagious pathogen causing the common cold (34), CoVs also contribute to approximately 15% of all cases of colds (35). As it has been shown that Zn^{2+} can inhibit CoV M^{pro}s (12), we then cannot exclude the possibility that Zn^{2+} treatment might have an impact on CoV-associated common colds as well. Given the unique inhibition mode of Zn^{2+} on CoV M^{pro}s, it displays the potential to be used as an adjunct therapy to treat CoV-associated diseases.

ACKNOWLEDGMENTS

REFERENCES

1. Lee N, Hui D, Wu A, Chan P, Cameron P, Joynt GM, Ahuja A, Yung MY, Leung CB, To KF, Lui SF, Szeto CC, Chung S, Sung JJ. 2003. A major outbreak of severe acute respiratory syndrome in Hong Kong. N Engl J Med 348:1986–1994. http://dx.doi.org/10.1056/NEJMoa030685.

2. Zaki AM, van Boheemen S, Bestebroer TM, Osterhaus AD, Fouchier RA. 2012. Isolation of a novel coronavirus from a man with pneumonia in Saudi Arabia. N Engl J Med 367:1814–1820. http://dx.doi.org/10.1056/NEJMoa1211721.

3. Kipar A, Meli ML. 2014. Feline infectious peritonitis still an enigma? Vet Pathol Online 51:505–526. http://dx.doi.org/10.1177/0300985814522077.

4. Olsen CW. 1993. A review of feline infectious peritonitis virus: molecular biology, immunopathogenesis, clinical aspects, and vaccination. Vet Microbiol 36:1–37. http://dx.doi.org/10.1016/0378-1135(93)90126-R.

5. Perlman S. 1998. Pathogenesis of coronavirus-induced infections. Review of pathological and immunological aspects. Adv Exp Med Biol 440:503–513.

6. Dye C, Siddell SG. 2005. Genomic RNA sequence of feline coronavirus strain FIPV WSU-79/1146. J Gen Virol 86:2249–2253. http://dx.doi.org/10.1099/vir.0.80985-0.

7. Anand K, Ziebuhr J, Wadhwani P, Mesters JR, Hilgenfeld R. 2003. Coronavirus main proteinase (3CLpro) structure: basis for design of anti-SARS drugs. Science 300:1763–1767. http://dx.doi.org/10.1126/science.1085658.

8. Yang H, Yang M, Ding Y, Liu Y, Lou Z, Zhou Z, Sun L, Mo L, Ye S, Pang H, Gao GF, Anand K, Bartlam M, Hilgenfeld R, Rao Z. 2003. The crystal structures of severe acute respiratory syndrome virus main protease and its complex with an inhibitor. Proc Natl Acad Sci U S A 100:13190–13195. http://dx.doi.org/10.1073/pnas.1835675100.

9. Xue X, Yu H, Yang H, Xue F, Wu Z, Shen W, Li J, Zhou Z, Ding Y, Zhao Q, Zhang XC, Liao M, Bartlam M, Rao Z. 2008. Structures of two coronavirus main proteases: implications for substrate binding and antiviral drug design. J Virol 82:2515–2527. http://dx.doi.org/10.1128/JVI.02114-07.

10. Anand K, Palm GJ, Mesters JR, Siddell SG, Ziebuhr J, Hilgenfeld R. 2002. Structure of coronavirus main proteinase reveals combination of a chymotrypsin fold with an extra alpha-helical domain. EMBO J 21:3213–3224. http://dx.doi.org/10.1093/emboj/cdf327.

11. Zhao Q, Li S, Xue F, Zou Y, Chen C, Bartlam M, Rao Z. 2008. Structure of the main protease from a global infectious human coronavirus, HCoV-HKU1. J Virol 82:8647–8655. http://dx.doi.org/10.1128/JVI.00298-08.

12. Lee CC, Kuo CJ, Hsu MF, Liang PH, Fang JM, Shie JJ, Wang AH. 2007. Structural basis of mercury- and zinc-conjugated complexes as SARS-CoV 3C-like protease inhibitors. FEBS Lett 581:5454–5458. http://dx.doi.org/10.1016/j.febslet.2007.10.048.

13. Zhang S, Zhong N, Ren X, Jin C, Xia B. 2011. 1H, 13C and 15N resonance assignments of SARS-CoV main protease N-terminal domain. Biomol NMR Assign 5:143–145. http://dx.doi.org/10.1007/s12104-010-9287-9.

14. Zhong N, Zhang S, Xue F, Kang X, Zou P, Chen J, Liang C, Rao Z, Jin C, Lou Z, Xia B. 2009. C-terminal domain of SARS-CoV main protease can form a 3D domain-swapped dimer. Protein Sci 18:839–844. http://dx.doi.org/10.1002/pro.76.

15. Barrila J, Gabelli SB, Bacha U, Amzel LM, Freire E. 2010. Mutation of Asn28 disrupts the dimerization and enzymatic activity of SARS 3CL(pro). Biochemistry 49:4308–4317. http://dx.doi.org/10.1021/bi1002585.

16. Hu T, Zhang Y, Li L, Wang K, Chen S, Chen J, Ding J, Jiang H, Shen X. 2009. Two adjacent mutations on the dimer interface of SARS coronavirus 3C-like protease cause different conformational changes in crystal structure. Virology 388:324–334. http://dx.doi.org/10.1016/j.virol.2009.03.034.

17. Hegyi A, Friebe A, Gorbalenya AE, Ziebuhr J. 2002. Mutational analysis of the active centre of coronavirus 3C-like proteases. J Gen Virol 83:581–593. http://dx.doi.org/10.1099/0022-1317-83-3-581.

18. Wang J, Wang F, Tan Y, Chen X, Zhao Q, Fu S, Li S, Chen C, Yang H. 2014. Crystallization and preliminary crystallographic study of feline infectious peritonitis virus main protease in complex with an inhibitor. Acta Crystallogr F Struct Biol Commun 70:1612–1615. http://dx.doi.org/10.1107/S2053230X14022390.

19. Otwinowski Z, Minor W. 1997. Processing of X-ray diffraction data collected in oscillation mode. Methods Enzymol 276:307–326. http://dx.doi.org/10.1016/S0076-6879(97)76066-X.

20. McCoy AJ, Grosse-Kunstleve RW, Adams PD, Winn MD, Storoni LC, Read RJ. 2007. Phaser crystallographic software. J Appl Crystallogr 40:658–674. http://dx.doi.org/10.1107/S0021889807021206.

21. Winn MD, Ballard CC, Cowtan KD, Dodson EJ, Emsley P, Evans PR,

Keegan RM, Krissinel EB, Leslie AG, McCoy A, McNicholas SJ, Murshudov GN, Pannu NS, Potterton EA, Powell HR, Read RJ, Vagin A, Wilson KS. 2011. Overview of the CCP4 suite and current developments. Acta Crystallogr D Biol Crystallogr 67:235–242. http://dx.doi.org/10.1107/S0907444910045749.

22. Adams PD, Afonine PV, Bunkoczi G, Chen VB, Davis IW, Echols N, Headd JJ, Hung LW, Kapral GJ, Grosse-Kunstleve RW, McCoy AJ, Moriarty NW, Oeffner R, Read RJ, Richardson DC, Richardson JS, Terwilliger TC, Zwart PH. 2010. PHENIX: a comprehensive Python-based system for macromolecular structure solution. Acta Crystallogr D Biol Crystallogr 66:213–221. http://dx.doi.org/10.1107/S0907444909052925.

23. Yang H, Xie W, Xue X, Yang K, Ma J, Liang W, Zhao Q, Zhou Z, Pei D, Ziebuhr J, Hilgenfeld R, Yuen KY, Wong L, Gao G, Chen S, Chen Z, Ma D, Bartlam M, Rao Z. 2005. Design of wide-spectrum inhibitors targeting coronavirus main proteases. PLoS Biol 3:e324. http://dx.doi.org/10.1371/journal.pbio.0030324.

24. Copeland RA. 2000. Enzymes: a practical introduction to structure, mechanism, and data analysis, 2nd ed. Wiley, New York, NY.

25. Vu TT, Fredenburgh JC, Weitz JI. 2013. Zinc: an important cofactor in haemostasis and thrombosis. Thromb Haemost 109:421–430. http://dx.doi.org/10.1160/TH12-07-0465.

26. Jacobsen FE, Lewis JA, Cohen SM. 2007. The design of inhibitors for medicinally relevant metalloproteins. ChemMedChem 2:152–171. http://dx.doi.org/10.1002/cmdc.200600204.

27. Katz BA, Clark JM, Finer-Moore JS, Jenkins TE, Johnson CR, Ross MJ, Luong C, Moore WR, Stroud RM. 1998. Design of potent selective zinc-mediated serine protease inhibitors. Nature 391:608–612. http://dx.doi.org/10.1038/35422.

28. Mahdi F, Madar ZS, Figueroa CD, Schmaier AH. 2002. Factor XII interacts with the multiprotein assembly of urokinase plasminogen activator receptor, gC1qR, and cytokeratin 1 on endothelial cell membranes. Blood 99:3585–3596. http://dx.doi.org/10.1182/blood.V99.10.3585.

29. Singh M, Das RR. 2013. Zinc for the common cold. Cochrane Database Syst Rev 6:CD001364. http://dx.doi.org/10.1002/14651858.CD001364.pub4.

30. Eby GA, Davis DR, Halcomb WW. 1984. Reduction in duration of common colds by zinc gluconate lozenges in a double-blind study. Antimicrob Agents Chemother 25:20–24. http://dx.doi.org/10.1128/AAC.25.1.20.

31. Maggini S, Beveridge S, Suter M. 2012. A combination of high-dose vitamin C plus zinc for the common cold. J Int Med Res 40:28–42. http://dx.doi.org/10.1177/147323001204000104.

32. Science M, Johnstone J, Roth DE, Guyatt G, Loeb M. 2012. Zinc for the treatment of the common cold: a systematic review and meta-analysis of randomized controlled trials. CMAJ 184:E551–E561. http://dx.doi.org/10.1503/cmaj.111990.

33. Korant BD, Kauer JC, Butterworth BE. 1974. Zinc ions inhibit replication of rhinoviruses. Nature 248:588–590. http://dx.doi.org/10.1038/248588a0.

34. Turner RB. 2001. The treatment of rhinovirus infections: progress and potential. Antiviral Res 49:1–14. http://dx.doi.org/10.1016/S0166-3542(00)00135-2.

35. To KK, Hung IF, Chan JF, Yuen KY. 2013. From SARS coronavirus to novel animal and human coronaviruses. J Thorac Dis 5(Suppl 2):S103–S108. http://dx.doi.org/10.3978/j.issn.2072-1439.2013.06.02.